International Forum on Aeroelasticity and Structural Dynamics
IFASD 2019
9-13 June 2019, Savannah, Georgia, USA

TAKEOFF DYNAMICS OF FLEXIBLE AIRCRAFT WITH MULTIPLE UNDERWING POD-MOUNTED LANDING GEARS

Antônio B. Guimarães Neto[1]

[1]Instituto Tecnológico de Aeronáutica
São José dos Campos, SP, 12228-900, Brazil
antonio@ita.br

Keywords: aeroelasticity, flight dynamics, flexible aircraft, takeoff, ground effect

Abstract: Formulations for the flight dynamics of flexible aircraft have been commonly applied to aircraft having all six rigid-body degrees of freedom unconstrained. However, during takeoff and landing, the aircraft motion becomes constrained by the ground. An intricate dynamical problem arises when the flexible aircraft has multiple underwing pod-mounted landing gears. During liftoff, the most outboard landing gears become airborne earlier than the most inboard ones. The equations of motion used in a simulation model must then include time-varying ground constraint forces. Aerodynamically, the ground effect becomes relevant and can be modeled using the method of images. Wheel-to-ground rolling resistance also needs to be considered. This paper aims at the derivation of equations of motion that allow simulating the takeoff of such complex aircraft configurations. The developed formulation is important because it is readily applicable also to the landing phase, allowing the calculation of landing loads and the design of takeoff and landing control systems with less uncertainties. As spinoffs, the stability analysis of flexible aircraft in ground effect and evaluation of takeoff performance are also made possible.

1 INTRODUCTION

A formulation for the flight dynamics of flexible aircraft using general body axes was proposed by Guimarães Neto et al. [1] In the formulation, small elastic deformations are assumed and a finite-element representation of the aircraft structure together with a lumped-mass representation of its properties of inertia are considered available. In the equations of motion (EOMs), the origin of the body axes is at a generic point O not necessarily coincident with the center of gravity (CG) of the aircraft. Moreover, in the case of dually-constrained axes [1], the origin S of the structural axes (point of no elastic displacement) is a material point (and structural node) that can be non-coincident with the origin O of the body axes.

The equations of motion derived in Ref. [1] and elsewhere [2–9] usually apply to aircraft that are free to fly in the three-dimensional space, having all six rigid-body degrees of freedom (DOFs) unconstrained. However, if the flexible aircraft is in contact with the ground, constraints must be applied to the landing gears, affecting the elastic deformation of the structure. Moreover, during takeoff and landing, the aerodynamic ground effect becomes relevant and must be modeled.

It is known that high-altitude, long-endurance (HALE) unmanned aerial vehicles have mission profiles that demand high-aspect-ratio wings [9]. Typically, several landing gears are mounted at underwing pods that are also used to carry instrumentation, flight control system components, batteries and, possibly, electrical motors. An example of such configuration is the NASA Helios

Prototype, shown in Fig. 1, with five pod-mounted fixed landing gears, each comprising two wheels in tandem.

Retrieved from: https://www.nasa.gov/sites/default/files/images/370828main_ED01-0209-1_full.jpg

Figure 1: The NASA Helios Prototype moments after takeoff (Credits: NASA photo).

Depending on how many wheels are in contact with the ground, the aircraft rigid-body motion can be constrained in a different number of degrees of freedom. For instance, with one wheel touching the ground, the vertical translation becomes constrained and a normal reaction force develops at the constraint, together with a rolling resistance force. This constraint also modifies the structural dynamics. As more wheels touch the ground, aircraft pitching and rolling also become constrained.

The aerodynamic ground effect adds to the complexity of this dynamical problem. If the flexible aircraft aerodynamics is modeled using the vortex-lattice (VLM) [10] or the doublet-lattice (DLM) [11] methods, then the ground effect can be approximately modeled using the method of images [12]. The dependence of the aerodynamic model on height above ground is then introduced, increasing the number of independent variables used in the aerodynamic look-up tables.

It is well known that the solution to the problem of trimming an aircraft with wheel-to-ground constraints and under the influence of the aerodynamic ground effect is possible in software like MSC Nastran [13], with the solution based on the formulation derived by Rodden and Love [14]. However, this paper aims at deriving a formulation that makes time-marching simulations of takeoff and landing of flexible aircraft possible, including aerodynamic nonlinearities in look-up tables and taking into account the nonlinear EOMs in the rigid-body DOFs.

The EOMs for flexible aircraft with multiple underwing pod-mounted landing gears, subjected to different ground constraints, are derived in this paper. Models for the ground effect and for wheel-to-ground rolling resistance are included. The EOMs are derived using Lagrange's equations with holonomic constraints [15, 16]. Similar constraints were already used before by Guimarães Neto et al. in Ref. [17], which dealt with the response and stability of a remotely-piloted flexible aircraft in wind-tunnel tests, with at least the aircraft rigid-body translational DOFs constrained.

The formulation derived in this paper can allow an accurate evaluation of takeoff field length, whenever accurate aerodynamic and rolling resistance models are available. The formulation also allows numerically testing different rotation strategies for safer operation. Stability analysis of flight in ground effect also become possible, allowing the prediction of potential degradation of handling qualities in the landing phase, which is known to be critical for such flexible aircraft. For instance, poor Dutch roll damping is very objectionable to the pilot in the approach for landing, and an adequate flight dynamics model for this flight phase can help in the mitigation of problems. Moreover, the formulation also makes possible the calculation of landing loads for aircraft of the type under consideration, making it useful in structural design.

The developed formulation is applied in this paper to the six-meter-span X-HALE aircraft configuration [18]. Designed at the University of Michigan, the aircraft was also built and is currently in operation by ITA (Instituto Tecnológico de Aeronáutica, Portuguese for Aeronautics Institute of Technology) in Brazil. Numerical results are shown and analyzed for equilibrium and stability under the influence of ground effect, for static equilibrium on ground, and for takeoff and landing simulations.

2 EQUATIONS OF MOTION OF THE CONSTRAINED AIRCRAFT

The equations of motion derived in this section are based on the assumption that the flexible aircraft has $n_c \geq 0$ constraints applied by the ground to wheels of its landing gears. The EOMs are then derived using Lagrange's equations with n_c holonomic constraints [15, 16]:

$$\frac{d}{dt}\left(\frac{\partial \mathcal{L}}{\partial \dot{q}_i}\right) - \frac{\partial \mathcal{L}}{\partial q_i} + \frac{\partial \mathcal{F}}{\partial \dot{q}_i} = \sum_{c=1}^{n_c} \lambda_c \frac{\partial f_c}{\partial q_i} + Q_i, \tag{1}$$

where $\mathcal{L} = T - U$ is the Lagrangian, T is the kinetic energy and U the potential energy; $\mathcal{F}$ is Rayleigh's dissipation function; f_c, $c = 1, 2, \cdots, n_c$, are the functions describing the constraints of the system; λ_c are the corresponding Lagrange multipliers; q_i, $i = 1, 2, \cdots, 6 + n$, are the $6 + n$ generalized coordinates of the system; and Q_i are the corresponding non-conservative generalized forces.

The generalized coordinates q_i constitute a vector $\mathbf{q}$. By definition, the holonomic constraints depend only on the generalized coordinates and time:

$$f_c = f_c(\mathbf{q}, t) = 0, \quad c = 1, 2, \cdots, n_c. \tag{2}$$

The body reference frame (BRF) has its set of orthonormal basis vectors forming the columns of a matrix $\mathfrak{F}_b$, which is then an orthogonal matrix. The Earth is assumed to define an inertial reference frame (IRF). The IRF orthonormal basis vectors are assumed to form the identity matrix: $\mathfrak{F}_0 = \mathbf{I}_3$. The transformation matrix from the IRF coordinate system to the BRF system is then given by:

$$\mathbf{C}_{b0} = \mathfrak{F}_b{}^T \mathfrak{F}_0, \tag{3}$$

and it can be obtained by a classical sequence (3-2-1) of Euler rotations, with the Euler angles ψ, θ and ϕ [19].

The elected set of $6 + n$ generalized coordinates for the flight dynamics of the flexible aircraft comprises: the components of the position vector $\mathbf{R}_{O,b}$ of the origin O of the BRF, expressed in the body axes, b: $\mathbf{R}_{O,b} = \begin{bmatrix} x_O & y_O & z_O \end{bmatrix}^T$; the Euler angles ψ, θ, and ϕ; and n elastic DOFs, constituting the displacement vector $\mathbf{u}_G = \begin{Bmatrix} u_1 & u_2 & \cdots & u_n \end{Bmatrix}^T$.

Important details regarding the derivation of the EOMs are now provided. For a more in-depth explanation of specific steps, the reader is referred to Ref. [1]. The position vector of any point I in the aircraft with respect to the origin of the IRF is expressed by:

$$\mathbf{R}_I = \mathbf{R}_O + \mathbf{s}_{OK} + \mathbf{s}_{KJ} + \mathbf{s}_{JI} + \mathbf{d}_{OK} + \mathbf{d}_{KJ} + \mathbf{d}_{JI}, \tag{4}$$

where $\mathbf{s}_{(\bullet)}$ refers to the relative position vectors in the undeformed (unstrained) condition, usually called the jig shape; and $\mathbf{d}_{(\bullet)}$ stands for the changes in the $\mathbf{s}_{(\bullet)}$ vectors due to the structural deformation. The point J is the center of mass (CM) of the jth mass element in a finite-element model that has lumped properties of inertia. There are N_m mass elements in the model. The CM of the jth mass element is rigidly attached to the structural node K.

The contact between any landing gear wheel and the ground is assumed, for simplification, to consist of a point, instead of an area. Then, let this point be denoted by L. The position vector of L is given by substituting L for I in Eq. (4), and can be written as:

$$\mathbf{R}_L = \mathbf{R}_O + \mathbf{r}_L. \tag{5}$$

The n_c constraints are obtained based on the simplifying assumption that the runway is plane and horizontal. The runway altitude above sea level is h_{runway}. If $\mathbf{e}_{n,i}$ denotes the ith column of the identity matrix of size n, $\mathbf{I}_n$, then any specific landing gear constraint in Lagrange's equations can be expressed by:

$$f_c = \mathbf{e}_{3,3}^T \mathbf{C}_{0b} \mathbf{R}_{L,b} + h_{\text{runway}} = 0, \tag{6}$$

where $\mathbf{C}_{0b} = \mathbf{C}_{b0}^T$ and $\mathbf{R}_L = \mathfrak{F}_b \mathbf{R}_{L,b}$.

In what refers to the rigid-body DOFs, Lagrange's equations (1) can be cast in a much more convenient form, using the inertial velocity vector components $\mathbf{V}_b = \begin{bmatrix} u & v & w \end{bmatrix}^T$ and the inertial angular velocity vector components $\boldsymbol{\omega}_b = \begin{bmatrix} p & q & r \end{bmatrix}^T$, both in the body system, as quasi-coordinates [15, 20]:

$$\begin{Bmatrix} \dfrac{d}{dt}\left(\dfrac{\partial T}{\partial \mathbf{V}_b}\right)^T \\ \dfrac{d}{dt}\left(\dfrac{\partial T}{\partial \boldsymbol{\omega}_b}\right)^T \end{Bmatrix} + \begin{bmatrix} \widetilde{\boldsymbol{\omega}_b} & \mathbf{0} \\ \widetilde{\mathbf{V}_b} & \widetilde{\boldsymbol{\omega}_b} \end{bmatrix} \begin{Bmatrix} \left(\dfrac{\partial T}{\partial \mathbf{V}_b}\right)^T \\ \left(\dfrac{\partial T}{\partial \boldsymbol{\omega}_b}\right)^T \end{Bmatrix} = \sum_{c=1}^{n_c} \begin{Bmatrix} \lambda_c \mathbf{C}_{b0} \mathbf{e}_{3,3} \\ \lambda_c \widetilde{\mathbf{r}_{L,b}} \mathbf{C}_{b0} \mathbf{e}_{3,3} \end{Bmatrix} + \begin{Bmatrix} \mathbf{F}_{a,b} + \mathbf{F}_{p,b} + \mathbf{F}_{rr,b} + m\mathbf{g}_b \\ \mathbf{M}_{a,O,b} + \mathbf{M}_{p,O,b} + \mathbf{M}_{rr,O,b} + m\widetilde{\mathbf{r}_{CG,b}}\mathbf{g}_b \end{Bmatrix}. \tag{7}$$

In Eq. (7), the skew-symmetric operator applied to a vector $\mathbf{v} = \begin{bmatrix} v_x & v_y & v_z \end{bmatrix}^T$ is equal to $\widetilde{\mathbf{v}} = v_x \left(\mathbf{e}_{3,3}\mathbf{e}_{3,2}^T - \mathbf{e}_{3,2}\mathbf{e}_{3,3}^T\right) + v_y \left(\mathbf{e}_{3,1}\mathbf{e}_{3,3}^T - \mathbf{e}_{3,3}\mathbf{e}_{3,1}^T\right) + v_z \left(\mathbf{e}_{3,2}\mathbf{e}_{3,1}^T - \mathbf{e}_{3,1}\mathbf{e}_{3,2}^T\right)$; $\mathbf{F}_{a,b}$, $\mathbf{F}_{p,b}$, and $\mathbf{F}_{rr,b}$ are the total aerodynamic, propulsive, and rolling resistance forces, respectively; $\mathbf{M}_{a,O,b}$, $\mathbf{M}_{p,O,b}$, and $\mathbf{M}_{rr,O,b}$ are the total aerodynamic, propulsive, and rolling resistance moments about the origin O, respectively; $\mathbf{g}_b$ is the gravity vector, assumed uniform over the airframe; and $\mathbf{r}_{CG,b}$ is the position vector of the deformed aircraft CG, coincident with the aircraft CM.

The other EOMs are those in the elastic DOFs, obtained from Eq. (1):

$$\frac{d}{dt}\left(\frac{\partial \mathcal{L}}{\partial \dot{u}_g}\right) - \frac{\partial \mathcal{L}}{\partial u_g} + \frac{\partial \mathcal{F}}{\partial \dot{u}_g} = \sum_{c=1}^{n_c} \lambda_c \frac{\partial f_c}{\partial u_g} + Q_g, \quad g = 1, \cdots, n. \tag{8}$$

To calculate the kinetic energy, the velocity vectors are expressed in terms of time derivatives taken in the IRF:

$$\begin{aligned} {}^0\dot{\mathbf{R}}_I = {}^0\dot{\mathfrak{F}}_b \left(\mathbf{R}_{O,b} + \mathbf{s}_{OK,b} + \mathbf{s}_{KJ,b} + \mathbf{s}_{JI,b} + \mathbf{d}_{OK,b} + \mathbf{d}_{KJ,b} + \mathbf{d}_{JI,b}\right) \\ + \mathfrak{F}_b \left({}^b\dot{\mathbf{R}}_{O,b} + {}^b\dot{\mathbf{d}}_{OK,b} + {}^b\dot{\mathbf{d}}_{KJ,b} + {}^b\dot{\mathbf{d}}_{JI,b}\right). \end{aligned} \tag{9}$$

The following equations were derived in Ref. [1] and are used in the present development:

$${}^0\dot{\mathfrak{F}}_b = \mathfrak{F}_b \widetilde{\boldsymbol{\omega}_b}, \tag{10}$$

$$\widetilde{\boldsymbol{\omega}_b} = \mathbf{C}_{b0}\dot{\mathbf{C}}_{b0}^T, \tag{11}$$

implying:

$${}^0\dot{\mathbf{R}}_I = \mathfrak{F}_b \left(\mathbf{V}_b + {}^b\dot{\mathbf{d}}_{OI,b} + \widetilde{\boldsymbol{\omega}_b}\mathbf{s}_{OI,b} + \widetilde{\boldsymbol{\omega}_b}\mathbf{d}_{OI,b}\right), \tag{12}$$

where $\mathbf{V}_b = {}^b\dot{\mathbf{R}}_{O,b} + \widetilde{\boldsymbol{\omega}_b}\mathbf{R}_{O,b}$, $\mathbf{s}_{OI,b} = \mathbf{s}_{OK,b} + \mathbf{s}_{KJ,b} + \mathbf{s}_{JI,b}$, and $\mathbf{d}_{OI,b} = \mathbf{d}_{OK,b} + \mathbf{d}_{KJ,b} + \mathbf{d}_{JI,b}$.

The elastic displacements of a node K are given by the translation vector $\mathbf{d}_K = \mathfrak{F}_b \mathbf{d}_{K,b}$ and by the Euler angle vector $\boldsymbol{\varphi}_{K,b} = \begin{bmatrix}\phi_{K,b} & \theta_{K,b} & \psi_{K,b}\end{bmatrix}^T$, with small deformations assumed, yielding:

$$\mathbf{d}_{OK,b} = \mathbf{d}_{K,b}, \tag{13}$$

$$\mathbf{d}_{KJ,b} = \widetilde{\boldsymbol{\varphi}_{K,b}}\mathbf{s}_{KJ,b}, \tag{14}$$

$$\mathbf{d}_{JI,b} = \widetilde{\boldsymbol{\varphi}_{K,b}}\mathbf{s}_{JI,b}. \tag{15}$$

The nodal displacements and rotations, $\mathbf{d}_{K,b}$ and $\boldsymbol{\varphi}_{K,b}$, can be recovered from the finite-element displacement vector, $\mathbf{u}_G$, with time-invariant Boolean matrices [1], $\mathbf{U}_{t,b,KG}$ and $\mathbf{U}_{r,b,KG}$, respectively:

$$\mathbf{d}_{K,b} = \mathbf{U}_{t,b,KG}\mathbf{u}_G, \tag{16}$$

$$\boldsymbol{\varphi}_{K,b} = \mathbf{U}_{r,b,KG}\mathbf{u}_G. \tag{17}$$

Then, as in Ref. [1], the kinetic energy becomes:

$$\begin{aligned} T = 1/2 \int_V {}^0\dot{\mathbf{R}}_I^T {}^0\dot{\mathbf{R}}_I \rho dV = 1/2 \sum_{j=1}^{N_m} \int_{V_j} {}^0\dot{\mathbf{R}}_I^T {}^0\dot{\mathbf{R}}_I \rho dV = \\ = 1/2\, m\mathbf{V}_b{}^T\mathbf{V}_b + 1/2\, \boldsymbol{\omega}_b{}^T \left(\mathbf{J}_{O,b} + \Delta\mathbf{J}_{O,b}\right)\boldsymbol{\omega}_b + 1/2\, \dot{\mathbf{u}}_G^T \mathbf{M}_{GG}\dot{\mathbf{u}}_G \\ -m\mathbf{V}_b{}^T \left(\widetilde{\mathbf{s}_{CG,b}} + \widetilde{\mathbf{d}_{CG,b}}\right)\boldsymbol{\omega}_b + m\mathbf{V}_b{}^T {}^b\dot{\mathbf{d}}_{CG,b} + \dot{\mathbf{u}}_G^T \mathbf{M}_{\boldsymbol{\omega}G}{}^T \boldsymbol{\omega}_b, \end{aligned} \tag{18}$$

where the summation of the contributions over N_m lumped-mass elements is implied, and:

$$\mathbf{J}_{O,b} = \frac{1}{2}\sum_{j=1}^{N_m} \left(m_j \widetilde{\mathbf{s}_{OJ,b}}^T \widetilde{\mathbf{s}_{OJ,b}} + \mathbf{J}_j\right), \tag{19}$$

$$\Delta\mathbf{J}_{O,b} = 2\sum_{j=1}^{N_m} m_j \left(\widetilde{\mathbf{s}_{OJ,b}}^T\widetilde{\mathbf{d}_{K,b}} + \widetilde{\mathbf{s}_{OK,b}}^T\mathbf{s}_{KJ,b}{\boldsymbol{\varphi}_{K,b}}^T - \widetilde{\mathbf{s}_{OJ,b}}^T\boldsymbol{\varphi}_{K,b}{\mathbf{s}_{KJ,b}}^T\right)$$
$$+\sum_{j=1}^{N_m} m_j \left(\widetilde{\mathbf{d}_{K,b}}^T\widetilde{\mathbf{d}_{K,b}} + 2\left(\widetilde{\mathbf{d}_{K,b}}^T\mathbf{s}_{KJ,b}{\boldsymbol{\varphi}_{K,b}}^T - \widetilde{\mathbf{d}_{K,b}}^T\boldsymbol{\varphi}_{K,b}{\mathbf{s}_{KJ,b}}^T\right)\right)$$
$$+\sum_{j=1}^{N_m}\left(\left(m_j\widetilde{\mathbf{s}_{KJ,b}}^T\widetilde{\mathbf{s}_{KJ,b}} + \mathbf{J}_j\right)\boldsymbol{\varphi}_{K,b}{\boldsymbol{\varphi}_{K,b}}^T\right)$$
$$+\sum_{j=1}^{N_m}\left(\widetilde{\boldsymbol{\varphi}_{K,b}}\left(2\mathbf{J}_j - \mathrm{tr}\left(\mathbf{J}_j\right)\mathbf{I}_3 - \widetilde{\boldsymbol{\varphi}_{K,b}}\left(m_j\mathbf{s}_{KJ,b}{\mathbf{s}_{KJ,b}}^T - \mathbf{J}_j + 1/2\ \mathrm{tr}\left(\mathbf{J}_j\right)\mathbf{I}_3\right)\right)\right), \tag{20}$$

$$\mathbf{M}_{GG} = \sum_{j=1}^{N_m} m_j \left({\mathbf{U}_{t,b,KG}}^T\mathbf{U}_{t,b,KG} - {\mathbf{U}_{t,b,KG}}^T\widetilde{\mathbf{s}_{KJ,b}}\mathbf{U}_{r,b,KG}\right.$$
$$\left.-{\mathbf{U}_{r,b,KG}}^T\widetilde{\mathbf{s}_{KJ,b}}^T\mathbf{U}_{t,b,KG}\right) + \sum_{j=1}^{N_m}{\mathbf{U}_{r,b,KG}}^T\left(m_j\widetilde{\mathbf{s}_{KJ,b}}^T\widetilde{\mathbf{s}_{KJ,b}} + \mathbf{J}_j\right)\mathbf{U}_{r,b,KG}, \tag{21}$$

$$\mathbf{s}_{CG,b} = \frac{1}{m}\sum_{j=1}^{N_m} m_j\left(\mathbf{s}_{OK,b} + \mathbf{s}_{KJ,b}\right), \tag{22}$$

$$\mathbf{d}_{CG,b} = \frac{1}{m}\sum_{j=1}^{N_m} m_j\left(\mathbf{U}_{t,b,KG} - \widetilde{\mathbf{s}_{KJ,b}}\mathbf{U}_{r,b,KG}\right)\mathbf{u}_G = \mathbf{D}_{CG,b}\mathbf{u}_G, \tag{23}$$

$${\mathbf{M}_{\boldsymbol{\omega}G}}^T = -\sum_{j=1}^{N_m}\left(m_j\left(\mathbf{U}_{t,b,KG} - \widetilde{\mathbf{s}_{KJ,b}}\mathbf{U}_{r,b,KG}\right)^T\widetilde{\mathbf{s}_{OJ,b}} - {\mathbf{U}_{r,b,KG}}^T\mathbf{J}_j\right)$$
$$-\sum_{j=1}^{N_m} m_j\left(\mathbf{U}_{t,b,KG} - \widetilde{\mathbf{s}_{KJ,b}}\mathbf{U}_{r,b,KG}\right)^T\mathrm{skew}\left(\mathbf{U}_{t,b,KG}\mathbf{u}_G - \widetilde{\mathbf{s}_{KJ,b}}\mathbf{U}_{r,b,KG}\mathbf{u}_G\right)$$
$$-\sum_{j=1}^{N_m}{\mathbf{U}_{r,b,KG}}^T\left(\widetilde{\mathbf{U}_{r,b,KG}\mathbf{u}_G}\left(-\mathbf{J}_j + 1/2\ \mathrm{tr}\left(\mathbf{J}_j\right)\mathbf{I}_3\right)\right)$$
$$= \overline{\mathbf{M}_{\boldsymbol{\omega}G}}^T + \Delta{\mathbf{M}_{\boldsymbol{\omega}G}}^T. \tag{24}$$

m_j is the mass and $\mathbf{J}_j$ is the inertia matrix of the jth lumped-mass element about its own center of mass. Comparing Eq. (7) with Eq. (18), the relation $\mathbf{r}_{CG,b} = \mathbf{s}_{CG,b} + \mathbf{d}_{CG,b}$ holds.

The elastic strain energy for the flexible aircraft modeled with finite elements reads:

$$U_{elas} = 1/2\left(\mathbf{T}_{FEM|BRF}\mathbf{u}_G\right)^T\mathbf{K}_{FEM}\left(\mathbf{T}_{FEM|BRF}\mathbf{u}_G\right) = 1/2\ {\mathbf{u}_G}^T\mathbf{K}_{GG}\mathbf{u}_G, \tag{25}$$

where the finite-element method (FEM) model nodal displacements can be calculated in generic coordinate systems other than the flight-mechanics BRF coordinate system. The transformation matrices from the BRF to such coordinate systems are collected in the block-diagonal transformation matrix $\mathbf{T}_{FEM|BRF}$, such that the original FEM stiffness matrix, $\mathbf{K}_{FEM}$, is transformed to $\mathbf{K}_{GG} = {\mathbf{T}_{FEM|BRF}}^T\mathbf{K}_{FEM}\mathbf{T}_{FEM|BRF}$.

The gravitational potential energy is given by:

$$U_{grav} = -\sum_{j=1}^{N_m} \int_{V_j} \mathbf{g}^T \mathbf{R}_I \rho dV$$
$$= -m\mathbf{g}_b{}^T \left(\mathbf{R}_{O,b} + \mathbf{s}_{CG,b} + \mathbf{d}_{CG,b}\right). \tag{26}$$

At last, structural dissipation due to damping forces of viscous nature is assumed [21]:

$$\mathcal{F} = 1/2\ \dot{\mathbf{u}}_G^T \mathbf{B}_{GG} \dot{\mathbf{u}}_G. \tag{27}$$

2.1 Generalized forces

The generalized forces in the elastic DOFs comprise aerodynamic, propulsive, and rolling resistance forces acting on the aircraft, and they are calculated with the equation [21]:

$$Q_g = \int_V \mathbf{f}_I{}^T \frac{\partial \mathbf{R}_I}{\partial u_g} dV = \int_V \mathbf{f}_{I,b}{}^T \mathfrak{F}_b{}^T \left(\frac{\partial \mathfrak{F}_b}{\partial u_g} \mathbf{R}_{I,b} + \mathfrak{F}_b \frac{\partial \mathbf{R}_{I,b}}{\partial u_g} \right) dV = \int_V \mathbf{f}_{I,b}{}^T \frac{\partial \mathbf{R}_{I,b}}{\partial u_g} dV, \tag{28}$$

where $\mathbf{f}_I$ is the force vector per unit volume acting on the generic point I in the aircraft. The forces and moments in the rigid-body DOFs can be obtained from the derivations shown in Ref. [1], which are omitted here for brevity.

The propulsive forces can be modeled as concentrated thrust forces acting on the thrust center of each one of the N_E aircraft engines. Considering that a matrix $\mathbf{C}_{be}$ transforms the thrust force from an engine frame – whose x axis is aligned with the thrust line – to the body frame, one has the concentrated force $\mathbf{T}_{e,b} = \mathbf{C}_{be}\mathbf{e}_{3,1}T_e$ applied at a point E whose position vector with respect to O in the undeformed aircraft is $\mathbf{s}_{OE,b}$.

Every thrust center is also considered to be coincident with or rigidly connected to a structural node K_E in the FEM model of the aircraft, with associated Boolean matrices $\mathbf{U}_{t,b,K_EG}$ and $\mathbf{U}_{r,b,K_EG}$. The translations and the rotations of the thrust center are then given by the vectors $\mathbf{d}_{e,b} = \left(\mathbf{U}_{t,b,K_EG} - \widetilde{\mathbf{s}_{K_EE,b}}\mathbf{U}_{r,b,K_EG}\right)\mathbf{u}_G$ and $\boldsymbol{\varphi}_e = \mathbf{U}_{r,b,K_EG}\mathbf{u}_G$, respectively, with $\mathbf{s}_{K_EE,b}$ the position vector of the thrust center with respect to K_E.

Under small deformations, the thrust vector is $\mathbf{T}_{e,b} = \left(\mathbf{C}_{be} + \widetilde{\boldsymbol{\varphi}_e}\right)\mathbf{e}_{3,1}T_e$ and the thrust center is $\mathbf{s}_{OE,b} + \mathbf{d}_{e,b}$. The concentrated propulsive force can be represented as a distributed force by means of a three-dimensional Dirac's delta function [7].

The rolling resistance generalized forces can also be modeled as concentrated forces acting horizontally at the wheel-to-ground points of contact, whenever vertical reaction forces are nonzero. Every wheel point of contact L is considered to be coincident with or rigidly connected to a structural node K_L in the FEM model of the aircraft, with associated Boolean matrices $\mathbf{U}_{t,b,K_LG}$ and $\mathbf{U}_{r,b,K_LG}$. $\mathbf{s}_{K_LL,b}$ is the corresponding position vector. The rolling resistance force acts opposite to the direction of the landing gear velocity vector, with the corresponding unit vector given by $-\mathbf{e}_{v,c}$.

The aerodynamic forces can be simplified with the use of lifting-surface methods like the vortex-lattice method (VLM) [10] or the doublet-lattice method (DLM) [11]. Hence, the aerodynamic forces and moments are concentrated on a discrete set of N_P aerodynamic grid points, located

at the centroids of the VLM/DLM boxes (panels), with N_P equal to the number of boxes in the discretization of the aerodynamic model.

The structural displacements at the aerodynamic grid points are calculated with a linear transformation matrix $\mathbf{G}_{AG}$ that provides the vector of aerodynamic normal and rotational displacements, $\mathbf{u}_A$, from the structural displacements, $\mathbf{u}_G$: $\mathbf{u}_A = \mathbf{G}_{AG}\mathbf{u}_G$.

Each aerodynamic grid point has two degrees of freedom – plunge and pitch – and the length N_A of the $\mathbf{u}_A$ vector is then $N_A = 2N_P$. The vector containing the aerodynamic forces and moments at the aerodynamic grid points is $\mathbf{P}_A$. With this rationale and based on Eq. (28), the generalized force in each $u_g = {\mathbf{e}_{n,g}}^T\mathbf{u}_G$ DOF reads:

$$\begin{aligned} Q_g = {\mathbf{e}_{n,g}}^T{\mathbf{G}_{AG}}^T\mathbf{P}_A \\ +{\mathbf{e}_{n,g}}^T\sum_{e=1}^{N_E}\left(\mathbf{U}_{t,b,K_EG} - \widetilde{\mathbf{s}_{K_EE,b}}\mathbf{U}_{r,b,K_EG}\right)^T T_e\left(\mathbf{C}_{be}\mathbf{e}_{3,1} - \widetilde{\mathbf{e}_{3,1}}\mathbf{U}_{r,b,K_EG}\mathbf{u}_G\right) \\ +{\mathbf{e}_{n,g}}^T\sum_{c=1}^{n_c}\left(\mathbf{U}_{t,b,K_LG} - \widetilde{\mathbf{s}_{K_LL,b}}\mathbf{U}_{r,b,K_LG}\right)^T F_{rr,c}\left(-\mathbf{C}_{b0}\mathbf{e}_{v,c}\right), \end{aligned} \tag{29}$$

and each Q_g can be collected in a vector $\mathbf{Q}_G = \sum_{g=1}^{n}\mathbf{e}_{n,g}Q_g$ respecting the ordering of $\mathbf{u}_G$:

$$\begin{aligned} \mathbf{Q}_G = {\mathbf{G}_{AG}}^T\mathbf{P}_A + \sum_{e=1}^{N_E}\left(\mathbf{U}_{t,b,K_EG} - \widetilde{\mathbf{s}_{K_EE,b}}\mathbf{U}_{r,b,K_EG}\right)^T T_e\left(\mathbf{C}_{be}\mathbf{e}_{3,1} - \widetilde{\mathbf{e}_{3,1}}\mathbf{U}_{r,b,K_EG}\mathbf{u}_G\right) \\ + \sum_{c=1}^{n_c}\left(\mathbf{U}_{t,b,K_LG} - \widetilde{\mathbf{s}_{K_LL,b}}\mathbf{U}_{r,b,K_LG}\right)^T F_{rr,c}\left(-\mathbf{C}_{b0}\mathbf{e}_{v,c}\right). \end{aligned} \tag{30}$$

2.2 Equations of motion

The equations of motion for the constrained flexible aircraft can be obtained by the substitution of the energy expressions, Eqs. (18), (25) and (26); Rayleigh's dissipation function, Eq. (27); the holonomic constraints, Eq. (6); and the generalized forces, Eqs. (30), into Lagrange's equations, Eqs. (7) and (8). It is assumed in the derivation that no change in the aircraft mass with time occurs. The EOMs then read:

$$\begin{aligned} m\dot{\mathbf{V}}_b + m\widetilde{\boldsymbol{\omega}_b}\mathbf{V}_b - m\widetilde{\mathbf{s}_{CG,b}}\dot{\boldsymbol{\omega}}_b - m\widetilde{\boldsymbol{\omega}_b}\widetilde{\mathbf{s}_{CG,b}}\boldsymbol{\omega}_b + m\mathbf{D}_{CG,b}\ddot{\mathbf{u}}_G \\ +m\widetilde{\dot{\boldsymbol{\omega}}_b}\mathbf{D}_{CG,b}\mathbf{u}_G + 2m\widetilde{\boldsymbol{\omega}_b}\mathbf{D}_{CG,b}\dot{\mathbf{u}}_G + m\widetilde{\boldsymbol{\omega}_b}\widetilde{\boldsymbol{\omega}_b}\mathbf{D}_{CG,b}\mathbf{u}_G \\ = m\mathbf{g}_b + \mathbf{F}_{a,b} + \mathbf{F}_{p,b} + \mathbf{F}_{rr,b} + \sum_{c=1}^{n_c}\lambda_c\mathbf{C}_{b0}\mathbf{e}_{3,3}, \end{aligned} \tag{31}$$

$$\begin{aligned} \mathbf{J}_{O,b}\dot{\boldsymbol{\omega}}_b + \widetilde{\boldsymbol{\omega}_b}\mathbf{J}_{O,b}\boldsymbol{\omega}_b + m\widetilde{\mathbf{s}_{CG,b}}\left(\dot{\mathbf{V}}_b + \widetilde{\boldsymbol{\omega}_b}\mathbf{V}_b\right) + m\widetilde{\mathbf{D}_{CG,b}\mathbf{u}_G}\left(\dot{\mathbf{V}}_b + \widetilde{\boldsymbol{\omega}_b}\mathbf{V}_b\right) \\ +\Delta\mathbf{J}'_{O,b}\dot{\boldsymbol{\omega}}_b + \widetilde{\boldsymbol{\omega}_b}\Delta\mathbf{J}'_{O,b}\boldsymbol{\omega}_b + \Delta\dot{\mathbf{J}}'_{O,b}\boldsymbol{\omega}_b + \dot{\mathbf{M}}_{\boldsymbol{\omega}G}\dot{\mathbf{u}}_G + \mathbf{M}_{\boldsymbol{\omega}G}\ddot{\mathbf{u}}_G + \widetilde{\boldsymbol{\omega}_b}\mathbf{M}_{\boldsymbol{\omega}G}\dot{\mathbf{u}}_G \\ = m\widetilde{\mathbf{s}_{CG,b}}\mathbf{g}_b + m\widetilde{\mathbf{D}_{CG,b}\mathbf{u}_G}\mathbf{g}_b + \mathbf{M}_{a,O,b} + \mathbf{M}_{p,O,b} + \mathbf{M}_{rr,O,b} + \sum_{c=1}^{n_c}\lambda_c\widetilde{\mathbf{r}_{L,b}}\mathbf{C}_{b0}\mathbf{e}_{3,3}, \end{aligned} \tag{32}$$

$$\mathbf{M}_{GG}\ddot{\mathbf{u}}_G + \mathbf{B}_{GG}\dot{\mathbf{u}}_G + \mathbf{K}_{GG}\mathbf{u}_G + m\mathbf{D}_{CG,b}{}^T\left(\dot{\mathbf{V}}_b + \widetilde{\boldsymbol{\omega}_b}\mathbf{V}_b\right)$$
$$+\mathbf{M}_{\boldsymbol{\omega}G}{}^T\dot{\boldsymbol{\omega}}_b + 2\dot{\mathbf{M}}_{\boldsymbol{\omega}G}^T\boldsymbol{\omega}_b - \frac{1}{2}\sum_{g=1}^{n}\mathbf{e}_{n,g}\boldsymbol{\omega}_b{}^T\frac{\partial\Delta\mathbf{J}_{O,b}}{\partial u_g}\boldsymbol{\omega}_b$$
$$= m\mathbf{D}_{CG,b}{}^T\mathbf{g}_b + \mathbf{Q}_G + \sum_{c=1}^{n_c}\left(\mathbf{U}_{t,b,K_LG} - \widetilde{\mathbf{s}_{K_LL,b}}\mathbf{U}_{r,b,K_LG}\right)^T\lambda_c\mathbf{C}_{b0}\mathbf{e}_{3,3}. \tag{33}$$

In Eqs. (31), (32), and (33), $\Delta\mathbf{J}'_{O,b} = 1/2\ \left(\Delta\mathbf{J}_{O,b} + \Delta\mathbf{J}_{O,b}{}^T\right)$ is the symmetric inertia matrix increment, and all the time derivatives are taken in the BRF (the left superscript b was omitted for brevity). Moreover, the EOMs are also subjected to the constraints of Eq. (6), so that the number of equations and unknowns match, allowing the calculation of the Lagrange multipliers.

2.3 Aerodynamic formulation

The aerodynamic loads acting on the flexible aircraft can be calculated as the superposition of loads that would be obtained for a perfectly rigid airframe with the incremental loads due to structural deformation. In this paper, to obtain the generalized aerodynamic loads related to the structural motion, the VLM [10] is used. The aerodynamic formulation is totally analogous to the one described in Ref. [1], and is omitted for brevity.

2.4 Inertia relief

Since the stiffness matrix $\mathbf{K}_{GG}$ refers to an unrestrained three-dimensional structure, it is a positive semi-definite matrix, with rank $n-6$ and a null space consisting of the space spanned by six linearly-independent vectors [22]. Therefore, six linearly-independent rigid-body motions are allowed by the FEM formulation. This condition is not desired because the coordinates of the point O and the Euler angles were already considered to be the rigid-body DOFs of the flexible aircraft. Hence, six constraints are needed to further specify the body axes with regard to the structural displacements.

In this paper, the body axes are assumed to be dually-constrained axes [1]. In this case, the origin S of the structural axes (point of zero elastic displacement) can be non-coincident with the origin O of the body axes. Enforcing $\mathbf{u}_S = \mathbf{0}$ is only correct if the external forces applied to the structure are self-equilibrating. If inertia relief is considered, a self-equilibrating force system can be generated if the d'Alembert force vector corresponding to rigid-body accelerations is summed to the right-hand-side of Eq. (33). In Ref. [1], this was demonstrated to be equivalent to left multiply all the terms in Eq. (33) by the inertia-relief projection matrix, $\mathbf{P}_r$:

$$\mathbf{P}_r\mathbf{M}_{GG}\ddot{\mathbf{u}}_G + \mathbf{P}_r\mathbf{B}_{GG}\dot{\mathbf{u}}_G + \mathbf{P}_r\mathbf{K}_{GG}\mathbf{u}_G + m\mathbf{P}_r\mathbf{D}_{CG,b}{}^T\left(\dot{\mathbf{V}}_b + \widetilde{\boldsymbol{\omega}_b}\mathbf{V}_b\right)$$
$$+\mathbf{P}_r\mathbf{M}_{\boldsymbol{\omega}G}{}^T\dot{\boldsymbol{\omega}}_b + 2\mathbf{P}_r\dot{\mathbf{M}}_{\boldsymbol{\omega}G}^T\boldsymbol{\omega}_b - \frac{1}{2}\mathbf{P}_r\sum_{g=1}^{n}\mathbf{e}_{n,g}\boldsymbol{\omega}_b{}^T\frac{\partial\Delta\mathbf{J}_{O,b}}{\partial u_g}\boldsymbol{\omega}_b$$
$$= m\mathbf{P}_r\mathbf{D}_{CG,b}{}^T\mathbf{g}_b + \mathbf{P}_r\mathbf{Q}_G + \mathbf{P}_r\sum_{c=1}^{n_c}\left(\mathbf{U}_{t,b,K_LG} - \widetilde{\mathbf{s}_{K_LL,b}}\mathbf{U}_{r,b,K_LG}\right)^T\lambda_c\mathbf{C}_{b0}\mathbf{e}_{3,3}, \tag{34}$$

where $\mathbf{P}_r = \mathbf{I}_n - \mathbf{M}_{GG}\boldsymbol{\Psi}_{r,S}\left(\boldsymbol{\Psi}_{r,S}^T\mathbf{M}_{GG}\boldsymbol{\Psi}_{r,S}\right)^{-1}\boldsymbol{\Psi}_{r,S}^T$, and $\boldsymbol{\Psi}_{r,S}$ is the matrix of rigid-body modes of the FEM model having unit displacements or rotations of the node S.

2.5 Use of modes of vibration as shape functions

The modal superposition technique is generally a valid approach to solve dynamic problems involving the deformation of structures [21]. Mode shapes obtained from the undamped, linearized and conservative system can then be applied as shape functions in the solution of the structural-dynamic problem of the aeroelastic aircraft. In this paper, the elastic deformations around the initial equilibrium condition are represented by a superposition of the aircraft inertia-relieved constrained modes of vibration [1], $\Delta\mathbf{u}_G = \boldsymbol{\Phi}\boldsymbol{\eta}$.

The modal matrix $\boldsymbol{\Phi}$ is constant throughout the simulation, and consists of the modes calculated with the $\mathbf{P}_r$ matrix obtained when all six rigid-body modes are kept in $\boldsymbol{\Psi}_{r,S}$. However, the inertia-relief projection matrix is updated in Eq. (34) whenever a rigid-body DOF is added to or removed from the flexible aircraft by the ground constraints, as described in the next subsection. The consideration of inertia relief ensures that no support reaction will develop on unconstrained rigid-body DOFs [1].

2.6 Landing gear constraints

The wheel-to-ground constraints, given by Eq. (6), give rise to normal reaction forces at each point of contact. Considering Eq. (31), each normal reaction force is given by:

$$\mathbf{N}_{c,b} = \lambda_c \mathbf{C}_{b0} \mathbf{e}_{3,3}, \tag{35}$$

which is a vertical force in the IRF because the runway was assumed to be plane and horizontal.

According to Eq. (35), if $\lambda_c \geq 0$, then the normal force is null or has a down component in the IRF coordinate system. Hence, if $\lambda_c \geq 0$, it results that the f_c constraint should be inactive, because there are no physical means by which the ground would pull the aircraft down. Active constraints are only those that result in $\lambda_c < 0$.

Depending on the aircraft geometry and on the active constraints, the aircraft can have:

1. no DOF constrained, leading to:
$$\boldsymbol{\Psi}'_{r,S} = \boldsymbol{\Psi}_{r,S}$$
2. its vertical translational DOF constrained, if only one wheel is touching the ground, leading to:
$$\boldsymbol{\Psi}'_{r,S} = \begin{bmatrix} \boldsymbol{\Psi}_{r,S}\mathbf{e}_{6,1} & \boldsymbol{\Psi}_{r,S}\mathbf{e}_{6,2} & \boldsymbol{\Psi}_{r,S}\mathbf{e}_{6,4} & \boldsymbol{\Psi}_{r,S}\mathbf{e}_{6,5} & \boldsymbol{\Psi}_{r,S}\mathbf{e}_{6,6} \end{bmatrix}$$
3. its vertical translational DOFs constrained at two wheels that are side by side, therefore also constraining the rolling motion, leading to:
$$\boldsymbol{\Psi}'_{r,S} = \begin{bmatrix} \boldsymbol{\Psi}_{r,S}\mathbf{e}_{6,1} & \boldsymbol{\Psi}_{r,S}\mathbf{e}_{6,2} & \boldsymbol{\Psi}_{r,S}\mathbf{e}_{6,5} & \boldsymbol{\Psi}_{r,S}\mathbf{e}_{6,6} \end{bmatrix}$$
4. its vertical translational DOFs constrained at two wheels that are one behind the other, therefore also constraining the pitching motion, leading to:
$$\boldsymbol{\Psi}'_{r,S} = \begin{bmatrix} \boldsymbol{\Psi}_{r,S}\mathbf{e}_{6,1} & \boldsymbol{\Psi}_{r,S}\mathbf{e}_{6,2} & \boldsymbol{\Psi}_{r,S}\mathbf{e}_{6,4} & \boldsymbol{\Psi}_{r,S}\mathbf{e}_{6,6} \end{bmatrix}$$
5. its vertical translational DOFs constrained at three or more wheels that are side by side and also one behind the other, constraining both rolling and pitching motions, leading to:
$$\boldsymbol{\Psi}'_{r,S} = \begin{bmatrix} \boldsymbol{\Psi}_{r,S}\mathbf{e}_{6,1} & \boldsymbol{\Psi}_{r,S}\mathbf{e}_{6,2} & \boldsymbol{\Psi}_{r,S}\mathbf{e}_{6,6} \end{bmatrix}$$

In the foregoing equations, $\boldsymbol{\Psi}'_{r,S}$ is the rigid-body mode matrix that is to be effectively used in determining the inertia-relief projection matrix contained in Eq. (34).

In nonlinear time-marching simulations, the structural displacements become states of the system, in the form of modal coordinates. It is then necessary to obtain the first and second time derivatives of the equations of constraints, so that the constraints and their time derivatives themselves also become states of the system. Otherwise, the constraints cannot be correctly enforced, because in a time step only the derivatives $\dot{\mathbf{V}}_b$, $\dot{\boldsymbol{\omega}}_b$ and $\ddot{\boldsymbol{\eta}}$ can have their values altered.

The time derivative of the constraint equation (6) is given by:

$$\dot{f}_c = \mathbf{e}_{3,3}^T \dot{\mathbf{C}}_{0b} \mathbf{R}_{L,b} + \mathbf{e}_{3,3}^T \mathbf{C}_{0b} \dot{\mathbf{R}}_{L,b}. \tag{36}$$

From Eqs. (11) and (5), one obtains:

$$\dot{f}_c = \mathbf{e}_{3,3}^T \mathbf{C}_{0b} \left(\mathbf{V}_b + \dot{\mathbf{r}}_{L,b} + \widetilde{\boldsymbol{\omega}_b} \mathbf{r}_{L,b} \right). \tag{37}$$

The second time derivative of f_c is then given by:

$$\ddot{f}_c = \mathbf{e}_{3,3}^T \mathbf{C}_{0b} \left(\dot{\mathbf{V}}_b + \widetilde{\boldsymbol{\omega}_b} \mathbf{V}_b + \ddot{\mathbf{r}}_{L,b} + 2\widetilde{\boldsymbol{\omega}_b} \dot{\mathbf{r}}_{L,b} + \widetilde{\dot{\boldsymbol{\omega}}_b} \mathbf{r}_{L,b} + \widetilde{\boldsymbol{\omega}_b} \widetilde{\boldsymbol{\omega}_b} \mathbf{r}_{L,b} \right). \tag{38}$$

Equation (37) is used to evaluate the time derivative of the states f_c and Eq. (38) is used to calculate the constraints at each time step. The calculation of $\dot{\mathbf{V}}_b$, $\dot{\boldsymbol{\omega}}_b$, $\ddot{\mathbf{u}}_G$, $\ddot{f}_c$, and λ_c is simultaneous. If $\lambda_c \geq 0$, then the cth constraint is inactive, and $\ddot{f}_c$ is allowed to be nonzero; if $\lambda_c < 0$, then the cth constraint is active, and $\ddot{f}_c = 0$. Depending on the active constraints, the inertia-relief projection matrix may need to be changed, according to the previously described procedure. The solution may then become iterative inside a time step.

2.7 Rolling resistance

Whenever a landing gear constraint is active, a rolling resistance (or rolling friction) force, $\mathbf{F}_{rr,c,b}$, tangent to the runway, can be included in the EOMs. Typically, the rolling resistance force is modeled as proportional (in magnitude) to the normal reaction force, with a constant of proportionality given by μ_r, the rolling resistance (or rolling friction) coefficient:

$$\|\mathbf{F}_{rr,c,b}\| = \mu_r \|\mathbf{N}_{c,b}\|. \tag{39}$$

In this paper, the rolling resistance force at a landing gear wheel is parallel to the runway, its magnitude is given by Eq. (39), and its direction is considered opposite to that of the velocity vector of the wheel-to-ground point of contact with respect to the IRF. For simplicity, the rolling resistance is considered to act only when such velocity vector is not null, implying that the aircraft will more easily start its motion from rest in the model than in reality.

The rolling friction coefficient depends on many factors such as the condition of the runway, the tire material, tread, pressure and loading, the condition of the wheel bearings and, to some extent, the speed [23]. Typical values can be found in Refs. [23, 24].

3 NUMERICAL MODEL

The aircraft analyzed in this paper is the six-meter-span X-HALE, a remotely-piloted flexible aircraft designed by Prof. Carlos Cesnik and coworkers at the University of Michigan [18], and currently also in operation by ITA in Brazil.

The six-meter-span configuration contains six wing sections with span of 1.0 m and chord of 0.2 m each, as well as five pods at the connections between the wing panels. Therefore, the wing aspect ratio is 30. At the pods, the aircraft electric motors, landing gears, electronics and sensors are installed. Booms are connected to the pods and, at the tip of each boom, a horizontal tail is mounted. The four side tails are all-moving control surfaces that can be used for both longitudinal and lateral-directional control, and are then named elevons. The central tail has a flipping-up capability, in order to modify the aircraft longitudinal and lateral-directional flying qualities as desired in operation. For ground clearance during takeoff, the central tail has approximately 33% less span in its right (bottom) part than in the left (top) part. The wing-tip sections have a dihedral angle of 10°. The wing is built with an incidence of 5°.

The aircraft has ten landing gears, two per pod. With the origin O of the body axes at the wing central node in the FEM model, with the body x_b axis oriented forward and the z_b axis downward, the front gears wheel-to-ground points of contact have x_b coordinate equal to 0.130 m and z_b coordinate equal to 0.224 m, whereas the rear gears have the x_b coordinate equal to -0.055 m and the same z_b coordinate.

Spring elements were included in the structural-dynamic model to approximately model the flexibility of the wheels. The vertical flexibility is considered as 1 centimeter of deformation for 10 Newtons of load, or 1000 N/m, more flexible than what observed – but not yet measured – in the real aircraft. The flexibility in other directions is numerically ten times higher. In the lack of experimental data, the rolling resistance coefficient is assumed as $\mu_r = 0.065$.

The aircraft structural-dynamic model consists of 144 beam elements along the wing span. The beam element formulation is as explained in Refs. [25, 26]. Beam elements are also used for the connection between the wing and the booms and for the booms themselves. The horizontal tails are modeled with rigid elements. Scalar spring elements are included to represent the stiffness of the motion of all the control surfaces around the corresponding hinge lines, but such stiffnesses are high enough not to modify the results to be obtained. The complete structural-dynamic model assembled in the ITA/AeroFlex program is shown in Fig. 2.

The mass of the aircraft is 12.2 kg. With respect to the wing central node, which is the origin of the body axes, the center of gravity is located at $\mathbf{s}_{CG,b} = \begin{bmatrix} -0.007 & -0.002 & 0.027 \end{bmatrix}^T$ meters.

In the time-marching simulations, stiffness-proportional structural damping is considered, with a constant of proportionality such that the first free-free mode of vibration has 1.5% damping ratio. Modes of vibration with frequency less than 51 Hz are retained – it was observed that the landing gear modes were between 50 and 51 Hz in the free-free model. The modal basis then has 46 modes, making the model more accurate in representing constraints that can significantly change during the simulation. A time step of 5 milliseconds is used for the simulations shown in this paper.

The aerodynamic model of the aircraft is based on the VLM [10], combined with the XFOIL code [27] to correct for viscous effects for both the wing EMX07 [18] and the elevons/horizontal

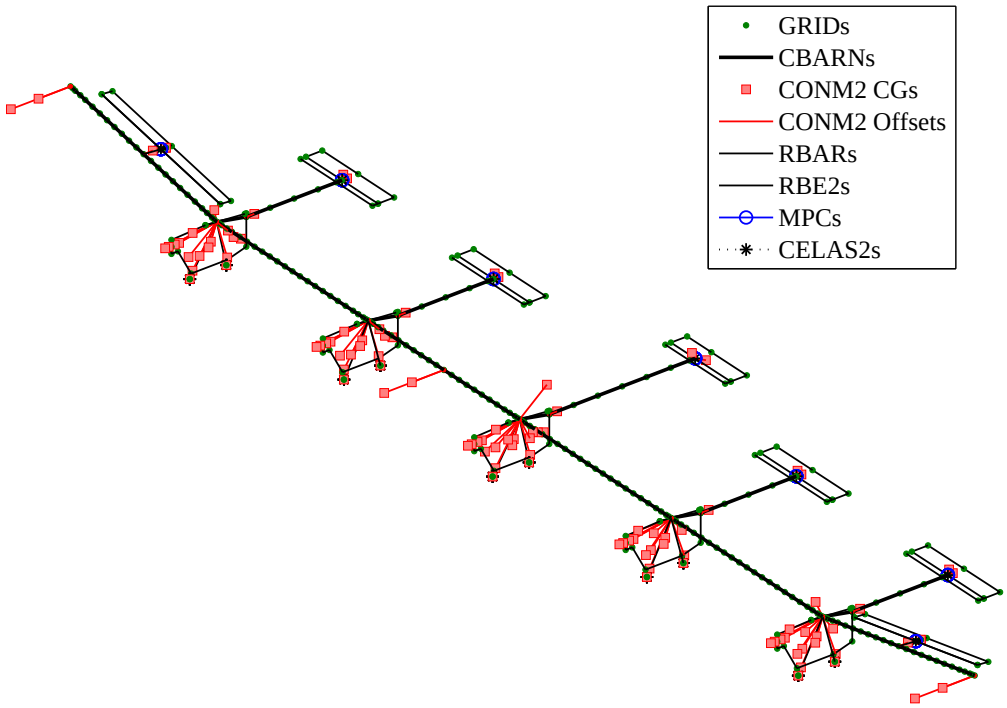

Figure 2: X-HALE six-meter-span configuration linear structural-dynamic model in ITA/AeroFlex. GRIDs: structural nodes; CBARNs: beam elements; RBARs: rigid bar elements; CONM2 CGs: CG locations of lumped-mass elements; CONM2 Offsets: offsets between such CG locations and the structural node to which the lumped-mass element is attached; CELAS2s: spring elements; and SUPORT: support location.

tail NACA 0012 airfoils. A local effective angle of attack is calculated for each strip of boxes in the VLM model, at each time step, considering the local airfoil incidence, the aircraft angle of attack and rigid-body motion, and the induced angle of attack calculated with the methodology of Ref. [28]. The effective angle of attack is then used to obtain airfoil coefficients and pressure coefficient distributions from look-up tables obtained off-line with XFOIL. Therefore, the aerodynamic model includes both finite-wing and nonlinear viscous aerodynamic effects. The viscous drag of aircraft components other than the lifting surfaces is calculated with semi-empirical methods.

The VLM mesh used in the aerodynamic model is shown in Fig. 3, and its refinement with 1674 boxes is due to its having been built to satisfy the guidelines of the doublet-lattice method [11, 29]. The aircraft has two ailerons, at the wing-tip modules.

Linear spline interpolation matrices, as derived in Ref. [13], are calculated and used to obtain the displacement-transferal and the load-transferal matrices between the structural-dynamic model and the aerodynamic model.

The propulsive model consists of a look-up table of thrust as a function of airspeed and throttle setting, based on experimental data obtained from wind tunnel tests. Linear interpolation is used both on airspeed and throttle setting to calculate thrust.

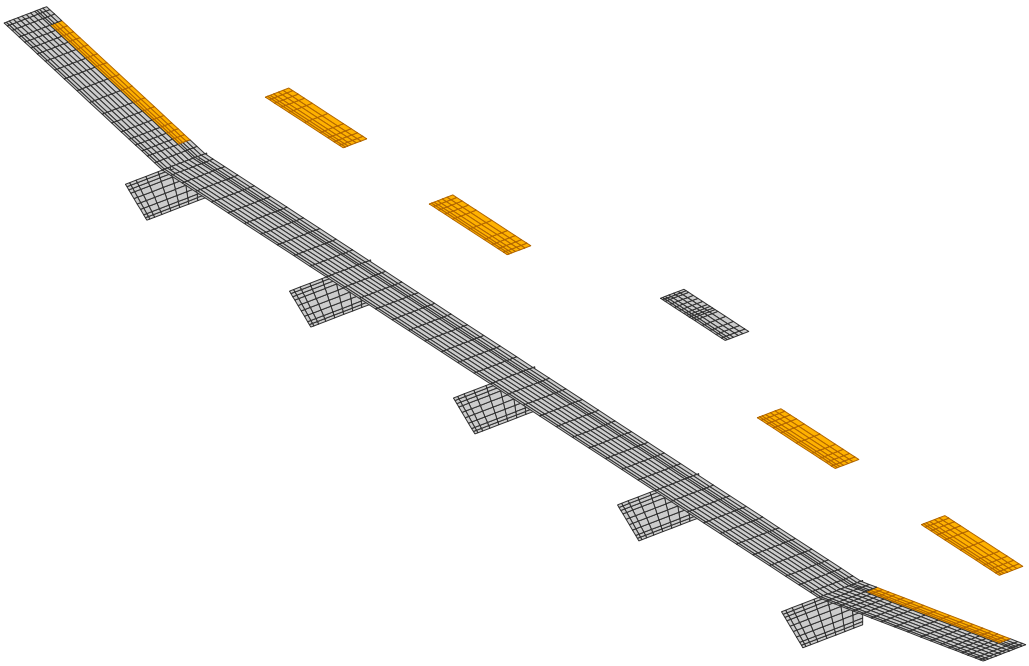

Figure 3: VLM mesh of the aircraft, with a total of 1674 boxes. Control surfaces are plotted in orange.

4 NUMERICAL RESULTS

4.1 Ground effect

In this paper, the ground effect is modeled using the method of images [12]. Because the aerodynamic model is a quasi-steady one, based on the VLM [10], unsteady flow phenomena that are potentially important [12] are not captured.

Regarding the rigid aircraft, results were obtained for the stability derivatives of lift and pitching moment coefficients with respect to the angle of attack, C_{L_α} and C_{m_α}, respectively. In the results shown in this section, the pitching moment is calculated about the origin of the ARF, located at the quarter-chord point of the wing symmetry plane. Figure 4 contains the results for the ratio of a derivative at a certain height above ground level (AGL) to the same derivative at an infinite height – that is, out of ground effect. The aircraft under analysis is the six-meter-span X-HALE with the central tail in the horizontal configuration.

One observes from Fig. 4 that the ground effect becomes more relevant the smaller the height above ground is compared with the wing span of six meters, without significant effects at heights greater than one wing span. Moreover, for the rigid aircraft, the effect is of greater magnitude on C_{m_α} than on C_{L_α}, because of the five horizontal tails downstream of the wing that are subjected to less downwash under ground effect. The neutral point would then tend to move rearward the closer the rigid aircraft was to the ground – the rearward shift is calculated to be 4.6% of the mean aerodynamic chord from $h_{AGL} \to \infty$ to $h_{AGL} = 0$.

To evaluate the influence of ground effect on the flexible aircraft, equilibrium conditions of straight level flight were then calculated for $V = 15$ m/s, at different values of h_{AGL}. The runway altitude is 650 m. Then, the aircraft equations of motion were linearized around the equilibrium condition. The linearized dynamics allowed the calculation of the C_{L_α} and C_{m_α} derivatives for the flexible aircraft subjected to quasi-static aeroelastic effects, according to the

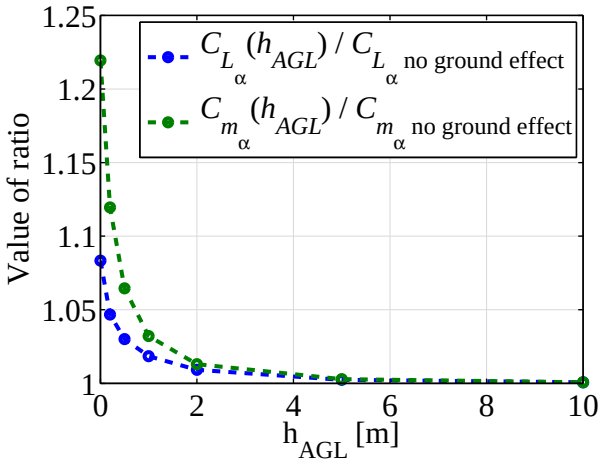

Figure 4: Ground effect on the C_{L_α} and C_{m_α} derivatives, for the rigid aircraft.

methodology of Ref. [30]. The determination of the natural modes was also possible. It was observed that all the aeroelastic modes are very slightly affected in both frequency and damping when under ground effect. The lateral-directional modes are also almost unaffected. The short-period and phugoid modes are more influenced. The results are summarized in Table 1.

Table 1: Equilibrium conditions and longitudinal modes at different values of h_{AGL}, for $V = 15$ m/s.

	h_{AGL} [m]					
	0.5	1.0	3.0	6.0	10.0	20.0
α_{eq} [deg]	1.48	1.54	1.61	1.64	1.65	1.66
$\delta_{e,eq}$ [deg]	-0.69	-0.52	-0.44	-0.42	-0.42	-0.43
$Thrust$ [N]	20.4	20.6	20.8	20.9	20.9	20.9
$\omega_{n,sp}$ [rad/s]	12.56	12.97	12.87	12.93	12.92	12.90
ζ_{sp}	0.495	0.500	0.506	0.503	0.503	0.503
$\omega_{n,ph}$ [rad/s]	0.541	0.601	0.688	0.692	0.692	0.692
ζ_{ph}	0.714	0.324	0.211	0.210	0.210	0.210
$C^{flex}_{m_\alpha}$ [1/rad]	-3.46	-3.55	-3.53	-3.51	-3.51	-3.51
$C^{flex}_{L_\alpha}$ [1/rad]	6.55	6.43	6.35	6.32	6.31	6.31

Table 1 shows that, because the ground effect allows more lift to be generated for the same angle of attack, the aircraft needs a smaller angle of attack to trim, α_{eq}, the closer it is to the ground. Because there is less downwash at the tails, the tail (elevator) deflection to trim, $\delta_{e,eq}$, is slightly in the direction of more trailing-edge up as height decreases. Because there is less induced drag, the total thrust to trim the aircraft is slightly smaller in ground effect.

The results for the short-period natural frequency $\omega_{n,sp}$ and damping ratio ζ_{sp} in Table 1 would at first seem counterintuitive, when compared with the trends in Fig. 4. However, one must have in mind that Fig. 4 holds for the rigid aircraft. In ground effect, the smaller aerodynamic downwash at the horizontal tails implies greater effectiveness and, for a flexible aircraft in which such tails are mounted on booms connected to the wing, the elastic twist produced by an increment in angle of attack can result in an effective aeroelastic downwash at very low h_{AGL} greater than the aerodynamic downwash out of ground effect. This is confirmed by the pitching moment coefficient derivative with quasi-static aeroelastic effects, $C^{flex}_{m_\alpha}$. The flexible aircraft

neutral point for $h_{AGL} = 0.5$ m can be calculated to be 2.8% of the mean aerodynamic chord forward of that for $h_{AGL} = 20.0$ m.

Table 1 also shows that the phugoid is the most affected mode. Its natural frequency $\omega_{n,ph}$ decreases and its damping ratio ζ_{ph} increases when the aircraft is closer to the ground.

4.2 Static equilibrium

At the beginning of the simulation of the takeoff run, the flexible aircraft needs to be in static equilibrium. This equilibrium condition was calculated, and it was found that, due to the flexibility included in the wheels, the aircraft has an equilibrium pitch attitude $\theta_{eq} = 4.89$ deg. This angle is positive because there is more vertical load at the rear landing gear wheels than at the front wheels. Table 2 shows the calculated normal reaction force on each wheel.

Table 2: Normal force on each landing gear wheel in static equilibrium.

	Normal force on wheel [N]				
	Left		Central	Right	
	Outer	Inner		Inner	Outer
Front	5.63	2.99	4.14	3.07	5.66
Rear	21.0	18.2	20.0	18.3	20.9

Having the y_b coordinate of each landing gear, it is possible to use the normal forces of Table 2 and estimate the $y_{CG,b}$ coordinate of the aircraft CG. The result is $y_{CG,b} = -0.002$ m, which, with the precision of millimeters, is the same as calculated from the known mass distribution of the model. This is then a valid experimental procedure to estimate the y_b coordinate of the CG, even with the aircraft being flexible. The same numerical test was performed and was unfortunately confirmed not to be valid for $x_{CG,b}$, because of the flexibility of the wheels. A more accurate experimental procedure would then probably require the removal of the very light flexible wheels for an adequate estimation of the CG location based on normal force measurement.

4.3 Takeoff simulation

With the aircraft starting at the static equilibrium condition, full throttle was applied at $t = 0.1$ s and a simulation of the takeoff dynamics was obtained using the formulation derived in this paper. The transfer function from commanded throttle to true throttle comprises a simple lag with time constant of 150 milliseconds, combined with a transport delay of 60 milliseconds, both estimated experimentally. The propulsive model was obtained via wind-tunnel tests. The deflections of control surfaces are zero throughout the simulation. The obtained results are shown in Figs. 5 and 6.

The time histories of the landing gear normal forces in Fig. 6 show that the aircraft lifts off slightly after $t = 4.37$ s, when the front central gear leaves the ground. The plots also confirm that the outer landing gears are the first to leave the ground, followed by the inner ones, and at last by the central ones. This is expected and consistent with the wing tip vertical displacements shown in Fig. 5. The takeoff is approximately symmetric, with the small asymmetries explained by both the small lateral offset of the CG (2 millimeters to the left) and the asymmetric horizontal central tail.

In the initial one to two seconds of the ground roll, the normal force on the front wheels increases with respect to the corresponding static equilibrium values, whereas the opposite occurs

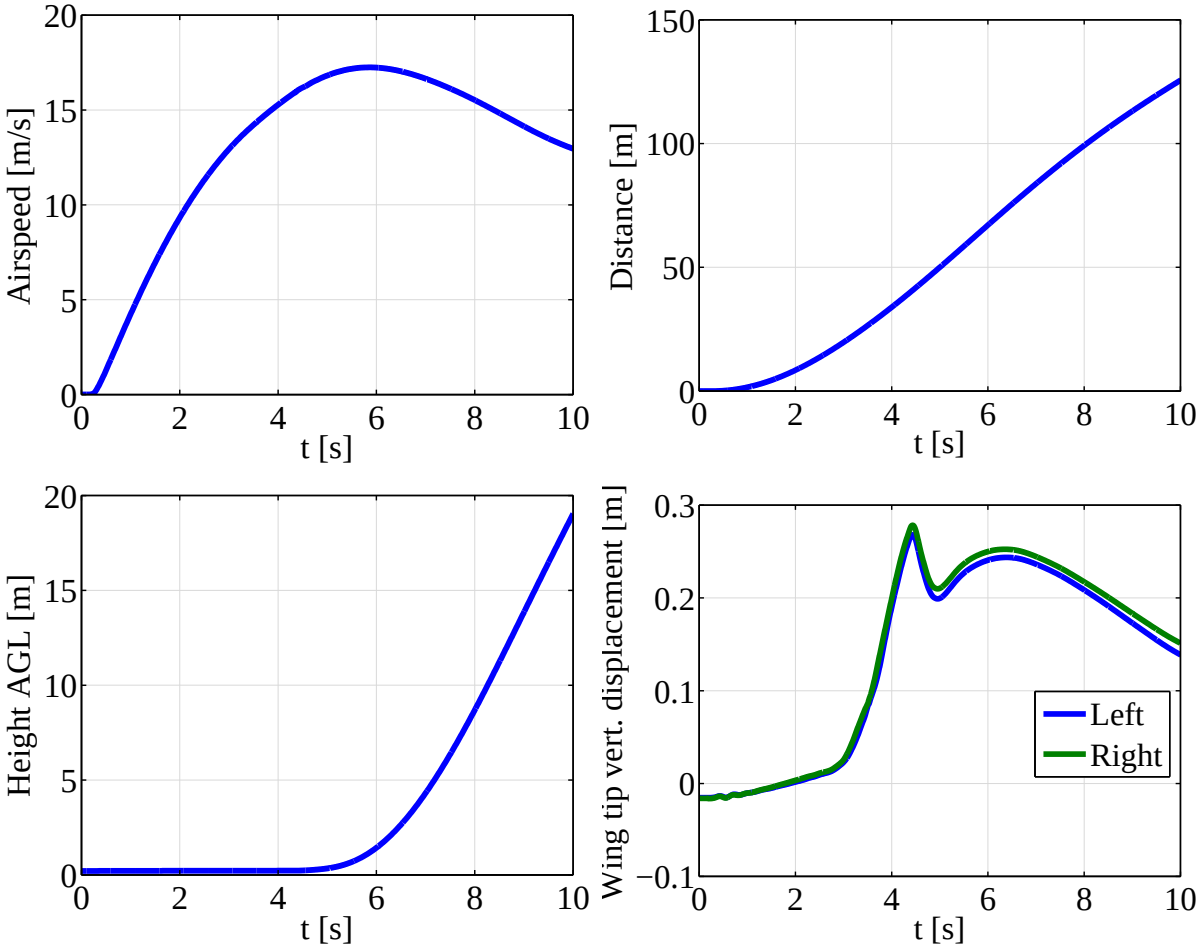

Figure 5: Takeoff dynamics of the X-HALE after a full-throttle command is applied, beginning at $t = 0.1$ s.

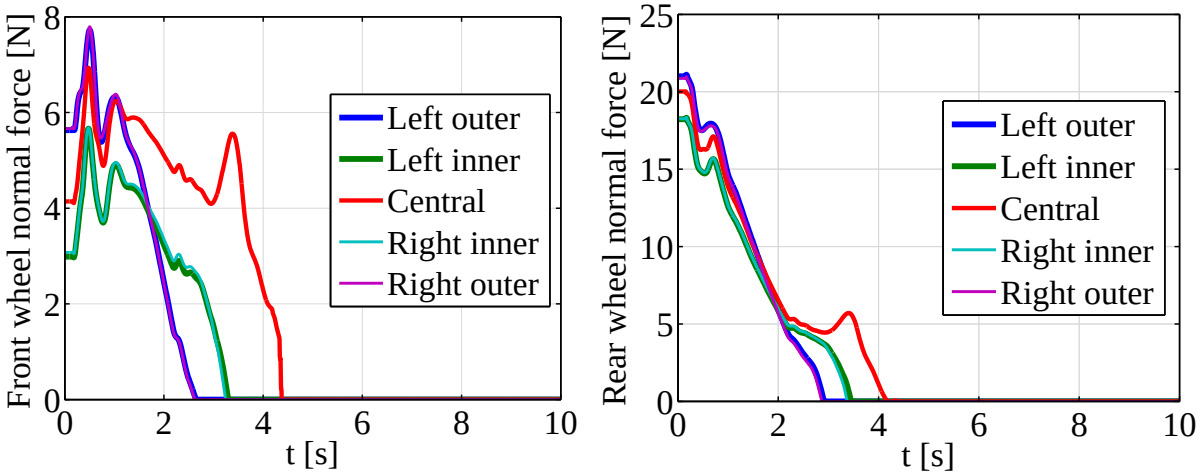

Figure 6: Landing gear wheels normal reaction forces during and after takeoff.

on the rear wheels. This is explained by the negative aerodynamic pitching moment that develops as airspeed increases. The liftoff without using elevator deflection occurs slightly before the aircraft attains $V = 16$ m/s. The distance traveled is approximately 40 meters until liftoff. This result can be affected by the value of the rolling friction coefficient, which was arbitrarily considered to be $\mu_r = 0.065$ in the simulations of this paper.

4.4 Simulation of landing without flare

The developed formulation is also applicable to the landing phase of flight. To illustrate this, the results of a simulation of landing without flare are shown in this section. The runway is assumed perfectly rigid. For the initial condition of the simulation, the aircraft was trimmed in a straight flight with a flight-path angle of -5 degrees at a height AGL of 15 meters. The simulated flight is approximately steady until the aircraft reaches about 2 meters AGL. The time histories of height AGL and pitch attitude, in the six seconds after reaching $h_{AGL} = 2$ m, are shown in Fig. 7. The normal reactions on the wheels, the normal load factors that would be measured by accelerometers installed in the aircraft, and the wing tip vertical displacements are shown in Fig. 8.

The aircraft does not land smoothly and has two unsuccessful touchdowns before finally landing. After the first touchdown, the throttle was set to zero. The unsuccessful touchdowns occur with the central wheels touching the ground, followed by the inner wheels and then the outer wheels, which are then the last to leave the ground. High normal load factors would be measured by the accelerometers when the outer landing gears strike the ground – such load factors are in a direction normal to the local wing plane.

The aircraft comes to a halt at $t = 14.0$ s, not shown in Figs. 7 and 8. This simulation is illustrative and considers the wheel flexibility modeled by springs with stiffness of 1000 N/m in the z_b axis direction. Moreover, the structural damping is a stiffness-proportional damping such that the first free-free mode of vibration of the aircraft has modal damping ratio of 1.5%. The actual wheels are probably less flexible but less damped, and adjustments of the model with experimental data are necessary before any correlation with flight-test data is intended.

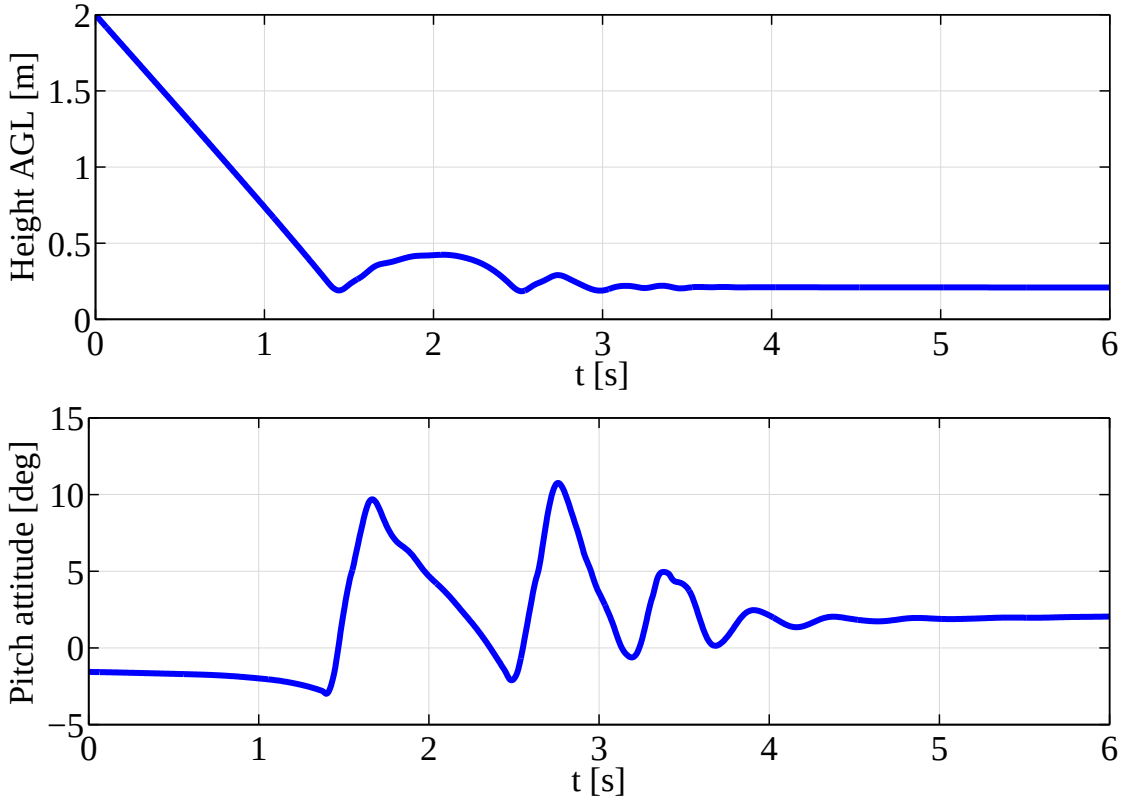

Figure 7: Height AGL and pitch attitude time histories in a landing without flare.

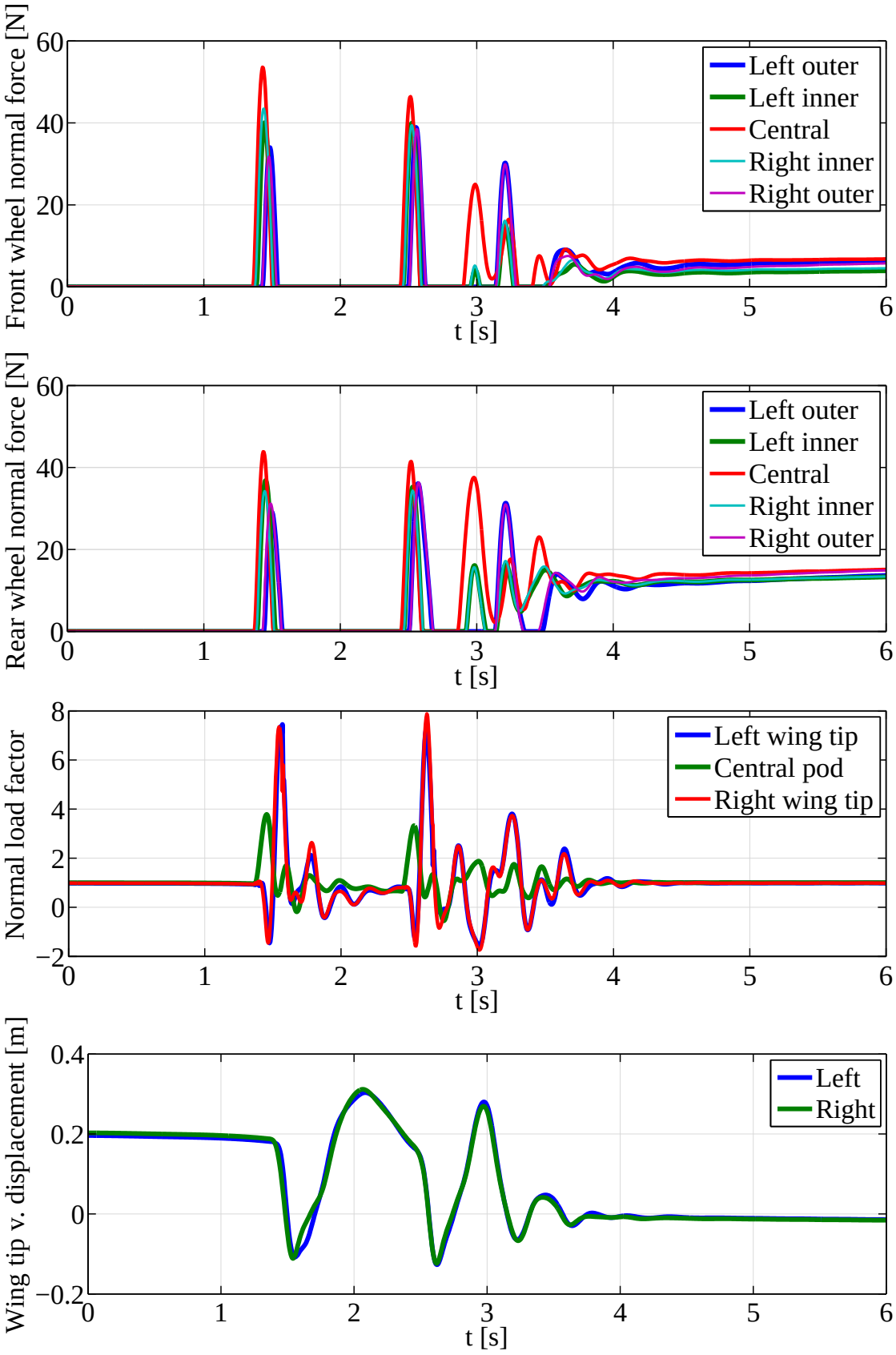

Figure 8: Normal reaction forces on wheels, normal load factors, and wing tip vertical displacements in a landing without flare.

5 CONCLUSIONS

In this paper, a formulation for the takeoff dynamics of flexible aircraft with multiple underwing pod-mounted landing gears was derived and the results of its application to the X-HALE aircraft were analyzed. In the derived equations of motion, small deformations were assumed, and the runway was assumed rigid, plane and horizontal. The proposed formulation includes the wheel-to-ground constraints, with both normal reaction and rolling resistance forces, as well as ground-effect aerodynamics.

The constraint dynamics are properly simulated with an on-line test of the active constraints, namely, those for which the constraint equation is satisfied and a normal force in the negative inertial z-axis direction exists. As the constraints become inactive during takeoff, modifications are made to the inertia-relief projection matrix to take into account only the rigid-body degrees of freedom that are unconstrained in the aircraft, until complete rigid-body freedom is attained at aircraft liftoff.

The aerodynamic model of the aircraft in this paper was simplified as a quasi-steady vortex-lattice-method model, instead of an unsteady doublet-lattice-method one that would have been more adequate to capture the unsteady effects in close proximity to the ground. The ground effect calculated with the quasi-steady model and the method of images is more significant for heights above ground on the order of a few wing chords. The wing-boom-tail type X-HALE flexible aircraft is subject to an aeroelastic downwash that leads to a decrease in the short-period natural frequency close to the ground, contrary to what would be expected for a rigid aircraft.

Using the developed formulation, the static equilibrium condition of the aircraft on the ground could be determined, including the normal forces applied on each landing gear wheel. The static equilibrium served as the initial condition for takeoff simulation, the results of which showed the expected behavior of the outer landing gears lifting off before the inner and then the central ones, which is also consistent with the wing deformation time history. An example of application to landing without flare was also analyzed, with significant structural loads developing.

Adjustments of the landing gear structural-dynamic model and of the rolling resistance coefficient are still necessary before any correlation with X-HALE flight-test data is intended. The developed formulation is readily applicable to simulations of takeoff and landing in gusty environments, which then require coupling with a control augmentation system or a human pilot model in order to produce meaningful results.

6 REFERENCES

[1] Guimarães Neto, A. B., Silva, R. G. A., Paglione, P., and Silvestre, F. J. (2016). Formulation of the flight dynamics of flexible aircraft using general body axes. *AIAA Journal*, 54(11), 3516–3534. doi:10.2514/1.J054752.

[2] Bisplinghoff, R. L., Ashley, H., and Halfman, R. L. (1955). *Aeroelasticity*. Cambridge: Addison-Wesley Publishing Company, Inc.

[3] Etkin, B. (1959). *Dynamics of Flight: Stability and Control*. New York: John Wiley & Sons, Inc.

[4] Bisplinghoff, R. L. and Ashley, H. (1962). *Principles of Aeroelasticity*. New York: Wiley & sons.

[5] Waszak, M. R. and Schmidt, D. K. (1988). Flight dynamics of aeroelastic vehicles. *Journal of Aircraft*, 25(6), 563–571. doi:10.2514/3.45623.

[6] Cesnik, C. E. S. and Brown, E. L. (2002). Modeling of high aspect ratio active flexible wings for roll control. In *43rd AIAA/ASME/ASCE/AHS/ASC Structures, Structural Dynamics, and Materials Conference*. Denver, CO. doi:10.2514/6.2002-1719. AIAA Paper 2002-1719.

[7] Meirovitch, L. and Tuzcu, I. (2004). Unified theory for the dynamics and control of maneuvering flexible aircraft. *AIAA Journal*, 42(4), 714–727. doi:10.2514/1.1489.

[8] Shearer, C. M. (2006). *Coupled nonlinear flight dynamics, aeroelasticity and control of very flexible aircraft*. Ph.D. thesis, University of Michigan, Ann Arbor. PhD in Aerospace Engineering.

[9] Shearer, C. M. and Cesnik, C. E. (2007). Nonlinear flight dynamics of very flexible aircraft. *Journal of Aircraft*, 44(5), 1528–1545. doi:10.2514/1.27606.

[10] Hedman, S. G. (1965). Vortex lattice method for calculation of quasi steady state loadings on thin elastic wings. Tech. Rep. 105, Aeronautical Research Institute of Sweden, Stockholm.

[11] Albano, E. and Rodden, W. P. (1969). A doublet-lattice method for calculating lift distributions on oscillating surfaces in subsonic flows. *AIAA Journal*, 7(2), 279–285. doi:10.2514/3.5086.

[12] Nuhait, A. O. (1995). Unsteady ground effects on aerodynamic coefficients of finite wings with camber. *Journal of Aircraft*, 32(1), 186–192. doi:10.2514/3.46699.

[13] Rodden, W. P. and Johnson, E. H. (1994). *MSC.NASTRAN Aeroelastic Analysis User's Guide*. MacNeal-Schwendler Corporation, Los Angeles.

[14] Rodden, W. P. and Love, J. R. (1985). Equations of motion of a quasisteady flight vehicle utilizing restrained static aeroelastic characteristics. *Journal of Aircraft*, 22(9), 802–809. doi:10.2514/3.45205.

[15] Meirovitch, L. (2003). *Methods of analytical dynamics*. Mineola, NY: Dover Publications, Inc.

[16] Flannery, M. R. (2005). The enigma of nonholonomic constraints. *American Journal of Physics*, 73(3), 265–272. doi:10.1119/1.1830501.

[17] Guimarães Neto, A. B., Silvestre, F. J., Bussamra, F. L. S., Silva, R. G. A., and Cesnik, C. E. S. (2017). Response and stability of the remotely-piloted, constrained X-HALE aircraft in wind tunnel. In *International Forum on Aeroelasticity and Structural Dynamics (IFASD) 2017*. Como, Italy. IFASD-2017-081.

[18] Cesnik, C. E. S., Senatore, P. J., Su, W., Atkins, E. M., and Shearer, C. M. (2012). X-HALE: A very flexible unmanned aerial vehicle for nonlinear aeroelastic tests. *AIAA Journal*, 50(12), 2820–2833. doi:10.2514/1.J051392.

[19] Stevens, B. and Lewis, F. (2003). *Aircraft Control and Simulation*. Wiley. ISBN 9780471371458.

[20] Meirovitch, L. (1991). Hybrid state equations of motion for flexible bodies in terms of quasi-coordinates. *Journal of Guidance, Control, and Dynamics*, 14(5), 1008–1013. doi: 10.2514/3.20743.

[21] Bismarck-Nasr, M. N. (1999). *Structural Dynamics in Aeronautical Engineering*. AIAA Education Series. Reston, VA: AIAA. ISBN 9781563473234. doi:10.2514/4.862458.

[22] Mantegazza, P. (2011). Tutorial on attached-mean axes and their use in the calculation of deformable static and damped-undamped vibration modes of a free-free structure. *Journal of Aeroelasticity and Structural Dynamics*, 2(1), 81–98.

[23] Vinh, N. X. (1993). *Flight mechanics of high-performance aircraft*. Cambridge Aerospace Series. New York, NY: University Press. ISBN 0521478529.

[24] Roskam, J. (2007). *Airplane flight dynamics and automatic flight controls*. Lawrence: DARcorporation. ISBN 9781884885174. Part 1.

[25] Guimarães Neto, A. B., Silvestre, F. J., Cardoso-Ribeiro, F. L., Bussamra, F. L. S., Silva, R. G. A., and Cesnik, C. E. S. (2017). Validity of the assumption of small deformations in aircraft with different levels of structural flexibility. In *International Forum on Aeroelasticity and Structural Dynamics (IFASD) 2017*. Como, Italy. IFASD-2017-080.

[26] Guimarães Neto, A. B., Cardoso-Ribeiro, F. L., and Silvestre, F. J. (2018). Applicability of geometrically-linear structural-dynamic models for the flight dynamics of arbitrarily-flexible aircraft. In *31st Congress of the International Council of the Aeronautical Sciences (ICAS) 2018*. Belo Horizonte, Brazil. ICAS2018-0523.

[27] Drela, M. (1989). XFOIL: An analysis and design system for low reynolds number airfoils. In T. J. Mueller (Ed.), *Low Reynolds Number Aerodynamics*. Berlin, Heidelberg: Springer Berlin Heidelberg. ISBN 978-3-642-84010-4, pp. 1–12. doi:10.1007/978-3-642-84010-4_1.

[28] Kálmán, T. P., Giesing, J. P., and Rodden, W. P. (1970). Spanwise distribution of induced drag in subsonic flow by the vortex lattice method. *Journal of Aircraft*, 7(6), 574–576. doi:10.2514/3.44219.

[29] Rodden, W. P., Taylor, P. F., McIntosh, S. C., and Baker, M. L. (1999). Further convergence studies of the enhanced doublet-lattice method. *Journal of Aircraft*, 36(4), 682–688. doi: 10.2514/2.2511.

[30] Guimarães Neto, A. B. (2014). *Flight dynamics of flexible aircraft using general body axes: a theoretical and computational study*. Ph.D. thesis, Instituto Tecnológico de Aeronáutica, São José dos Campos, Brazil. PhD in Aeronautical and Mechanical Engineering.

ACKNOWLEDGMENT

This work has been supported in part by FINEP and EMBRAER under the research project Advanced Studies in Flight Physics, contract number 01.14.0185.00.

COPYRIGHT STATEMENT